Flexural and shear strengthening of RC beams reinforced with externally bonded CFRP laminates postfire exposure by experimental and analytical investigations

Flexural and shear strengthening of RC beams reinforced with externally bonded CFRP laminates postfire exposure by experimental and analytical investigations

Nestor Mejía[a,*], Andres Sarango[b], Alejandro Espinosa[b]

[a]*Department of Environment, Land and Infrastructure Engineering, Politecnico di Torino, Corso Duca degli Abruzzi, 24, 10129 Torino, Italy*
[b]*Department of Earth Sciences and Construction, University of the Armed Forces ESPE, Av. General Rumiñahui S/N, 171103, Sangolquí - Ecuador*

Abstract

As reinforcing structural systems in RC (reinforced concrete) elements are continually researched, more complex challenges in engineering are found that demand mathematical innovations that describe the composite elements' behaviour subject to different scenarios. The current study analyses the performance of RC beams reinforced with externally bonded carbon-fibre-reinforced polymer (CFRP) sheets postfire exposure regarding flexural, shear strengthening, and final state damage. In this sense, the progressive damage and changing of flexural/shear strengthening of different RC beams reinforced with CFRP laminates are tracked and measured in an experimental stage. Then, an analytical model is developed based on the results obtained in the previous phase. The study is divided into four sections: (a) ten RC beams were manufactured following a lab scale. Eight beams are reinforced with U-wraps and an externally bonded FRP laminate on the bottom face. Subsequently, a fire insulation material over the CFRP laminates is bonded to protect the CFRP from fire; (b) those beams were exposed to elevated temperatures for 60 min; (c) three-point flexural tests are conducted to track, characterize, and define the final

*Corresponding author. Phone: (39) 329-5519345, Email: nestor.mejiaalmeida@polito.it

state damage and the changing in flexural/shear strengthening; and (d) analytical models are developed to extend the study from lab-scale to actual scenarios. Validation studies proved that the model was reasonably accurate. Relevant findings include the following: (a) brittle behaviour is directly related to the crushing of compressive concrete and a curvature less than 0.1 m^{-1}; (b) the forming, triggering, and gradual propagation of multiple cracks are present in ductile failure; and (c) a major crack-forming trigger and instant propagation are present in brittle failure. Therefore, the findings reported in this study can be helpful in the structural reinforcement of buildings vulnerable to fire.
Keywords: reinforced concrete beams, carbon-fibre-reinforced polymers, final state damage, and flexural/shear strengthening.

1. Introduction

The United Nations (UN) stated on May 16, 2018, that 55% of the world's population resides in urban areas [1]. Thus, it has had a significant impact on the cost of living. In this sense, vulnerable groups such as people experiencing homelessness, immigrants, refugees, and the urban poor must live in settlements of improvised buildings known as shanty towns. One of the drawbacks of shanty towns is that their infrastructures are not constructed based on urban policies. By looking at the collection of all possible disaster risks, the fire hazard could be one. Therefore, government agencies have been regulating improvised buildings through structural analysis subject to elevated temperatures and subsequently with structural reinforcements to increase their load capacity and providing an appropriate fire resistance.

Concrete has excellent performance for long periods at high temperatures. It is due to its thermal properties, characterized by low thermal diffusion and high fire resistance.

On the other hand, the increase in temperature induces changes in the chemical composition and physical structure [2]. Concrete is generally obtained by mixing a Portland cement binder (chemically consisting of C_3S and C_2S, $Ca_3Al_2O_6$, C_4AF, and $CaSO_4$ [3]), water, aggregates, and other additives. The type of binder and quantity of cement define the concrete microstructure. The deterioration of concrete's mechanical properties is attributed to the changes in the chemical composition. In this sense, results have been reported. [4] et al. shows that the concrete starts to disintegrate due to the $Ca(OH)_2$ forming more hydrated products for temperatures over 400 °C. Temperatures over 600 °C trigger a transformation from Ca_2O_4Si to (C-S-H) gel. This chemical change causes a detrimental in the binding of the ingredients of concrete, carrying effects of crumbling concrete. Finally, Temperatures over 800 °C induce a detrimental effect on the concrete microstructure, causing a significant loss of material properties of the concrete. Additionally, [5] et al. stated that the concrete suffers a carbonation process where significant release of the chemically bound water from the calcium silicate hydrate (CSH) for temperatures above 110 °C. The concrete suffers micro-cracks for temperatures above 300 °C. It is because of the CSH's dehydration and the aggregates' thermal expansion. Temperatures around 530 °C provoke shrinkage in the concrete, causing irreversible damage. Regarding the effects of magnesium sulfate in concrete, this sulfate induces the formation of brucite that causes severe damage to concrete, such as cracking, spalling, strength reduction, increasing volumetric expansion, and mass loss [6].

While some concrete damages attributed to the changes in the physical structure are reported by [7]. The concrete cover presents visible, considerable, and extensible cracks at temperatures around 600, 800, and 1000 °C. The concrete cover is partially and fully

fragmented at 1200 °C. Therefore, the variation in these physical conditions directly infers a severe deterioration of the mechanical properties of concrete. [8] et al. reported that the compressive strength of concrete is detrimental at 5%, 15 – 40%, and 55 – 70% at temperatures around 250 °C, 300 °C, and 550 °C, respectively. Additionally, elevated temperatures in RC structural elements cause a diminishing load capacity, a dense cracking map in concrete, detrimental in the debond between reinforcing steel and concrete, and distort the steel; consequently, repairing these structural elements demands a cost greater than effectiveness [9]. Successively, after fire exposure, the concrete elements experience a rapidly cooling process. The temperature gradient produced between the concrete cover and concrete core producing a considerable tensile stress. Subsequently, it causes an expansion and contraction into aggregate and cement paste triggering cracks within concrete [10]. In addition, a substantial thermal gradient directly infers a shift in the line of action of the internal force (moving towards the cold side), causing the bending moment to inverse [11]. Therefore, the thermal gradient analysis on the cross-section should not be precluded because it directly affects the load-bearing capacity and, subsequently, the failure mode [12].

Throughout the years, several studies regarding the bending response of FRP-RC elements based on the wrapped/bonded technique have been performed. In general terms, [13] reported that the advantages of FRP-RC elements reinforced with the wrapped/bonded technique are superior shear and torsion performance and increased strength capacity and lifetime, while the disadvantages are its brittle debonding failure mode, the low glass transition temperature of epoxy resin and FRP laminate, and the adhesion between the reinforced element and the FRP laminate. The volumetric ratio and fiber orientation of

FRP directly influence the structural responses of RC members [14]. Thus, the wrapping configuration has been classified into one-sided bonding, complete wrapping, and U-wrap [15]. The RC beams reinforced with U-wrap considerably enlarged the plastic strain and withstood higher deflections and stresses than regular beams at a given load [14]. [16] et al. experimentally studied the effect of combined bending, shear, and torsion in RC beams reinforced with U-wraps. The results showed that the principal strain acts approximately 45° to the beam longitudinal axis, torsional cracks spread at approximately 50°, the U-wraps enlarge the torsional capacity by 70%, and the twisting moment has a negligible effect on the deflection. The percentage increase in the ductility and twist angle is ascribed to the configuration of FRP wrapping. At the same time, the type of fibre composite defined the enlargement of ultimate torque [17]. [18] et al. explored how the dimensions of FRP impact the shear performance of RC beams strengthened with CFRP U-strips and completely wrapped. The results showed that the predominant failure modes for U-strips are concrete crushing and debonding, while for wholly wrapped, it is rupture of CFRP. Other alternative reinforcement techniques have been implemented, such as externally bonded reinforcement on/in grooves (EBROG, EBRIG)), X-shaped, and T-shaped. [19] et al. revealed that such techniques postpone the debonding effects and increase the tensile capacity of FRP material, mid-span deflection, and load-carrying capacity. Additionally, the failure mode of specimens strengthened with EBROG/EBRIG (one layer) presented rupture in the FRP, while the EBROG/EBRIG (multiple layers) FRP presented concrete cover separation [21].

The transition towards reinforcing non-rectangular beams with FRP demands a more nuanced understanding of principles across mathematics, physics, and engineering. The

challenge lies in the non-uniform distribution of shear stresses over the height of the beams with non-rectangular cross-sections (such as L- or T-shaped) [20], unlike their rectangular counterparts. The non-uniform distribution of shear stresses can lead to localized high shear stress concentrations. Additionally, the variations in beam geometry cause differential strain profiles across the beam depth. Thus, the superposition of these aspects entails a mismatch in deformation between the CFRP and concrete, increasing the interfacial stresses and causing debonding. In this sense, some studies researched the structural performance of T-shaped beams reinforced with FRP laminates externally bonded. [22] developed a sophisticated detection method using piezoelectric sensors to monitor the debonding process between T-beams and FRP sheets precisely. This approach revealed that the piezoelectric sensor, positioned on the debonding regions, registers signal fluctuations. The results show that T-beams reinforced with FRP U-shape sheets along the web section of the beams increase their shear strength, but it also revealed the occurrence of premature debonding at small strain values. [23] et al. studied the anchorage mechanism of beams with T cross-section. The results showed that the ultimate load capacity in rectangular beams increased by 250%, 160%, and 210% for two longitudinal FRP patches on each side of the beam, flexural layer only, and two U-wraps, respectively. Additionally, the failure mode that evolved T- beams was the rupture of FRP for U-wraps while debonding for two others. On the other hand, Mofidi et al. concluded that the FRP contribution in T-beams in the ultimate load capacity is only highlighted when T-beams are not strengthened with internal transverse steel. [24] et al. proposed a numerical model for predicting the structural responses of RC T-beams reinforced with different wrapping configurations under combined torsion and shear. The results revealed that the complete

wrapping configuration is the most effective in terms of cracking torque, ultimate torque, and maximum angle of twist for the beams.

A significant hurdle of FRP-strengthened concrete structures under elevated temperatures is to avoid detrimental interfacial adhesion between FRP and concrete matrix. It depends on the individual properties and interaction between these materials and how external factors affect them. [25], [26] stated that a significant prolongation of heating time over the glass transition temperature (T_g) of the resin (adhesive substance) degrades FRP's mechanical properties. The service temperature for epoxy-bonded joints has been debated. For example, [25], [27], [28], and [29] limited the service temperature to 10, 15, 20, and 10-20 °C below the epoxy T_g, respectively. Due to concerns about the performance of FRPs at high temperatures, a fire insulation material over FRP laminates is necessary to protect them. Incorporating thermal mortars as insulators of elevated temperature has been conversant with the construction field. After elevated temperature exposure, the thermal mortals can keep their insulation properties, but their mechanical properties and internal structure experience deterioration [30]. [31] et al. employed a cementitious fire insulation material over FRP laminates to increase fire resistance time. The results show that the cementitious material protected FRP laminates but did not affect the adhesive agents. Furthermore, [32] et al. observed that high-temperature thermal properties of insulation should be included in the thermomechanical analysis because they directly depend on the temperature profile modeling of the cross-section. Subsequently, it significantly alters the final state of damage from FRP-RC members. A second-order effect experienced a thermal bowing phenomenon. It occurs when the differential heating on the cross-section is prominent.

The strengthening of RC beams by using FRP has been thoroughly studied. Nevertheless, there needs to be more information on the serviceability behaviour of RC beams reinforced with externally bonded FRP laminates exposed to elevated temperatures. In fact, there are vague and no definitive conclusions about the CFRP laminate deterioration caused by direct flame and its impact on the structural performance of RC beams. In this context, the predominant objective of the present research is to carry out such a study. It will include the influence of the wrapping configuration, insulation material, temperature gradient, and deterioration of the FRP's mechanical properties. The results will allow us to conduct structural reinforcement works appropriately using FRP external bonding techniques, keeping FRP's integrity at elevated temperatures. Additionally, this information could be helpful in a specific procedure for the fire design of RC structures reinforced with FRP composite.

2. Experimental study

2.1. Materials

2.1.1. Specimens

Ten RC beam specimens were manufactured (Fig.1). Each beam had identical dimensions of 12 x 18 x 150 cm and similar longitudinal and transverse reinforcement ratios of 1.58% and 0.69%, respectively. Two steel bars with a diameter of 8 mm were provided at the tension and compression zone. Five steel bars with a diameter of 8 mm were provided as the stirrups and distributed uniformly. Fig.2 depict the details of reinforcement steel configuration.

All beams were cast using the same commercial mixed concrete, with a compressive

strength of 210 kg/cm^2. It was obtained through the breaking of eight cylindrical concrete specimens. The thickness of the concrete cover was 30 mm. Furthermore, five K-type thermocouples are embedded and placed proportionally into the specimens to define the temperature distribution in the cross-section to study the cracking variations regarding temperature. In this sense, all beams were identically manufactured in materials, properties, and configurations.

(a) Steel Reinforcement (b) Thermocouple sensor (c) Cast concrete specimen

(d) Specimens (e) Cross-section

Fig. 1: Specimen fabrication process.

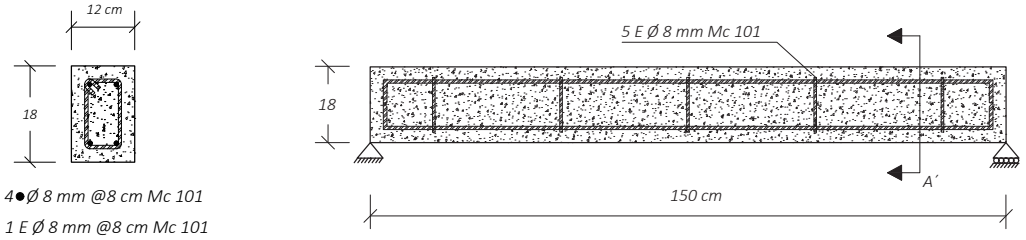

(a) Cross-section (b) Distribution along the specimen length

Fig. 2: Steel reinforcement details of specimens.

2.1.2. FRP material

A commercially available CFRP sheet, specifically the Tyfo® SCH-41 Composite, was employed to improve the test specimens' flexural strength, shear resistance, and/or ductility, as illustrated in Figure 3. Table 1 details the properties of the CFRP laminates. Two distinct CFRP retrofitting schemes were employed, guided by the principles outlined in the [27], "Guide for the Design and Construction of Externally Bonded FRP Systems for Strengthening Concrete Structures," published by the American Concrete Institute. The first retrofitting scheme involved applying a single CFRP layer bonded along the specimens' tension zone (Figure 4b) to enhance flexural capacity. Meanwhile, the second one utilized four U-shaped CFRP strips externally wrapped around three sides of each specimen (Figures 4a and c) to improve shear strength. These two schemes' principles and design methodologies are detailed in Chapters 10 and 11 of the [27].

Additionally, previous research, including studies by [3], [16], [33], [34] implemented the retrofitting schemes outlined in the [27]. In contrast, [31] integrated these two schemes such that the bonded U-shaped jacked increases the specimen's flexural strengthening and provides anchorage for the bonded longitudinal FRP, transforming them into tension-

carrying cables. Therefore, the present study guided by the results of the performance of the reinforced system under elevated temperatures as documented by [31], applying the retrofitting schemes depicted in Figure 4.

On the other hand, the longitudinal and U-shaped fiber strips were bonded to the beams using Sikadur® 301 epoxy resin. The optimum mix proportions and detailed preparation procedures are given by [35].

(a) Cleaning

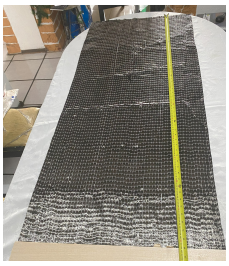

(b) Cutting to size

(c) FRP application

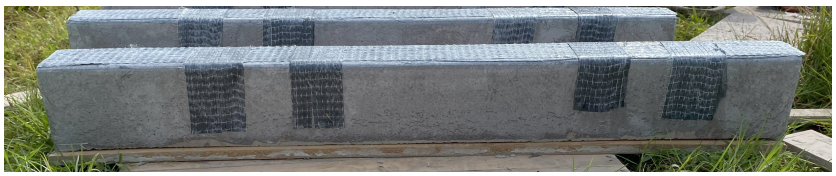

(d) Bonded along the specimen length

Fig. 3: Bonded details.

Table 1: Mechanical properties of the CFRP sheet [35].

Property	**Typical test value**
Tensile strength	620,000 psi (4.3 GPa)
Tensile modulus	36.0 x 10^6 psi (250 GPa)
Ultimate elongation	1.7%
Density	0.064 lbs./in^3 (1.77g/cm^3)

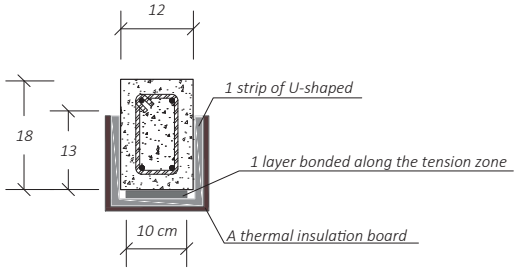

(a) Section B-B'

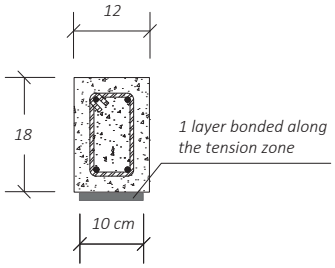

(b) Section A-A'

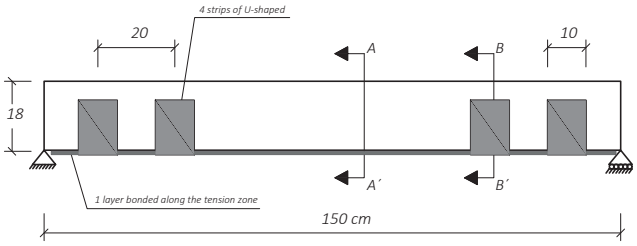

(c) Distribution along the specimen length

Fig. 4: CFRP schemes.

2.1.3. Fire protection material

In this study, one group of specimens reinforced with CFRP was protected from fire by a U-shaped insulation jacket (Fig. 5), while another group was left unprotected, identified respectively as Exp-A-x and Exp-A-y. The Exp-A-x group comprised four identical specimens. The insulation jacket utilized was crafted from a mixture of perlite, pumice, and cement, measuring 1 cm in thickness. Detailed specifications of the insulation material utilized in this study are outlined in Table 2.

The application of a U-shaped insulation jacket is specifically designed to serve exclusively as a thermal barrier, enhancing fire resistance. This thermal insulation method ensures that the resin, applied as an adhesive layer between the FRP reinforcement and the concrete matrix, remains below its glass transition temperature, preserving the integrity of

its mechanical interlocking. Additionally, this protective mortar jacket shields the CFRP strips from direct fire exposure, maintaining their structural integrity. It also plays a vital role in preventing the dehydration of the concrete, a process that could cause geometric discontinuities within the concrete substrate. Such distresses have the potential to trigger premature debonding in the reinforcement system, undermining its effectiveness.

(a) Applying the mortar

(b) First layer application

(c) Thickness

Fig. 5: Installing mortar insulation jackets.

Table 2: Chemical composition and physical properties of pumice aggregate [36].

Chemical composition		**Physical properties**	
Component	%		
SiO_2	70.50	Specific gravity (kg dm^{-3})	1.80
Al_2O_3	15	Bulk density (kg dm^{-3})	0.65
Fe_2O_3	3.5	Water absorption (%)	42
CaO	3.00		

2.2. Methodology

2.2.1. Nomenclature

To place this nomenclature on a more technical footing, the present study denominates the type of analysis with the abbreviation Exp (experimental) or Theo (theoretical). Subsequently, the specimens with or without FRP reinforcement are codified by the capital letter *A* or *B*. The lowercase letter *x* or *y* infers whether or not a thermal insulation board is attached. Finally, if the specimen is exposed to elevated temperatures, it is codified with the lowercase letter *a* followed by digits 01 to 04 (burning sequence). If the specimen is not exposed to elevated temperatures, it is codified with the lowercase letter *b*. The first experimental test, for example, is codified in terms of Exp-A-x-a-02, (Fig. 6).

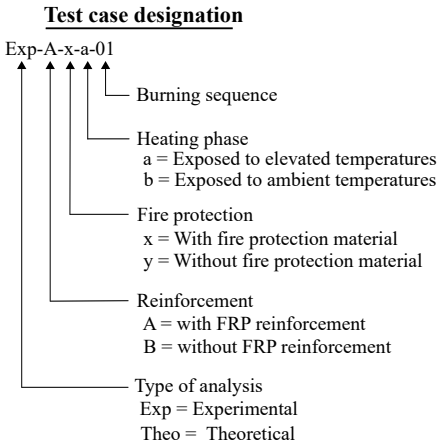

Fig. 6: Specimen and test case designations.

2.2.2. Heating phase

The first stage of the experimental test consists of fire tests conducted in the horizontal kiln (Fig. 7) of the Materials Laboratory of Civil Engineering Career of the University of the Armed Forces ESPE. The kiln was self-manufactured and can test horizontal structural

elements under static loads. A natural gas burner and firewood system generate the kiln heating. In this sense, eight specimens were tested according to the following sequence: (a) the specimen was placed into the kiln's chamber; (b) a distributed static load of 3.8 kN/m was applied to the specimen by a weight kit; (c) the specimens were exposed at different temperatures for one hour; (d) the temperature distribution of the cross-section was defined by temperature measurement using thermocouples; and (e) the specimen was cooled for 24 hours before the three-point bending flexural test.

(a) kiln

(b) Heating phase

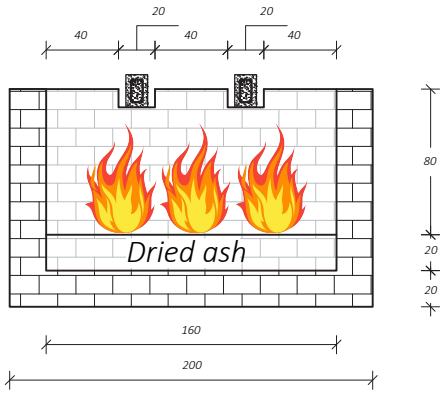

(c) Cross-section

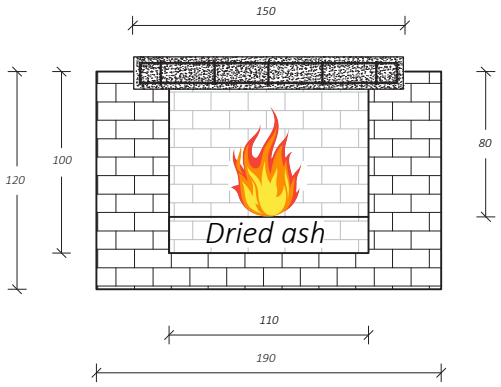

(d) Transversal-section

Fig. 7: Heating phase.

2.2.3. Test setup and instrumentation

Figure 8 shows the 3-point flexural test machine used during the experimental trials. The simple supported beam specimen was preloaded by a concentrated load of 0.2 kN at its centre. It was subsequently unloaded to guarantee the appropriate positioning between the machine and the specimen. Regarding instrumentation, a linear variable differential transducer LVDT (measuring range + 0.5 mm) was placed on the beams' rear face to record the vertical displacement at its centre. At the same time, a pressure sensor was mounted in the pneumatic jack to monitor the monotonically increasing axial load (loading rate of 5 kgf/s). High-speed filmmaking equipment (Canon EOS R8 and Phantom V2512) was located a short distance from the test apparatus and positioned level in height with the field of view between the beam's centre and the applied load's pressure sensor. The trial process was carried out through the following steps: (a) the pneumatic jack was turned on; (b) the pressure sensor and LVDT were checked to verify its correct operation; (c) the shear load was progressively transmitted to the specimen before the first crack appeared; (d) the camera was triggered; and (e) damage was tracked through digital images.

As described previously, ten RC beam specimens were manufactured, three of which were used to systematize and refine the experimental methodology through a trial and error process. Therefore, the experimental results were obtained through 7 trials.

(a) Test machine (b) Distribution along the specimen length

Fig. 8: Test setup and instrumentation.

2.2.4. *Preparation and image acquisition*

A grid of 25 tracking markers (15 x 30 cm^2) in terms of two-dimensional coordinates was marked in each specimen to obtain a displacement field at the frontal surface with 1% precision [37]. A set of two cameras (Canon EOS R8) and one camera (Phantom V2512) are synchronized in the focal length, resolution, and other settings to ensure a sequence homogeneity of triple videos. Subsequently, the videos are split into many images with a 4272 x 2848 pixels resolution.

2.2.5. *Data processing*

The digital images were binarized through a code that replaces the image pixels in values 1 (white) and 0 (black). After that, the tracked markers were identified and tracked using the Hough transform algorithm by circular shapes. Image processing is used to get the tracker markers' position regarding intrinsic coordinates (concerning the image's frame of reference). Subsequently, a projective transformation converts the tracker markers' position in intrinsic coordinates to world coordinates (concerning an external world

observer). It was based on the direct linear transformation (DLT) algorithm. Finally, the strain field of tracker markers is defined.

2.2.6. Validation

Fig. 9 shows the load-displacement curve obtained by LVDT at the mid-span in the experimental studies. It also compares with the results obtained by image processing data. Therefore, the correlating between the experimental studies and digital image processing results reveals that a grid of 25 tracking markers (15 x 30 cm^2) generates an average strain precision less than 1%.

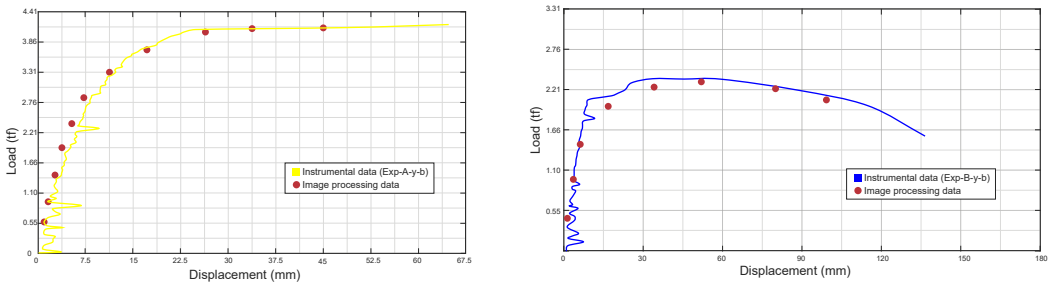

(a) Exp-A-y-b (b) Exp-B-y-b

Fig. 9: Validation between instrumental and experimental data.

2.2.7. Moment-curvature diagram

The moment-curvature diagrams are obtained through a code in which the experimental and image-processing data are sequenced and synchronized in time. The code relates to the moment through the shear and bending moment diagram. At the same time, the curvature is defined trigonometrically to the data acquired by the digital image processing (strain field) and the specimen geometry.

3. Analytical study

3.1. Mechanical behaviour of concrete

The Hognestad parabolic model (Fig. 10) describes the stress-strain relationship for unconfined concrete under compression, from its initial elasticity to ultimate strength and failure, highlighting its nonlinear behavior ([38], Section 2.1.4.4). The stress in the concrete σ_c up to the peak compressive strength $f_{co}^{'}$ is given by Eq. (1). Where ε_c, ε_{co}, and ε_{cu} denote the strain in concrete, the strain at peak stress, and the ultimate compressive strain, respectively.

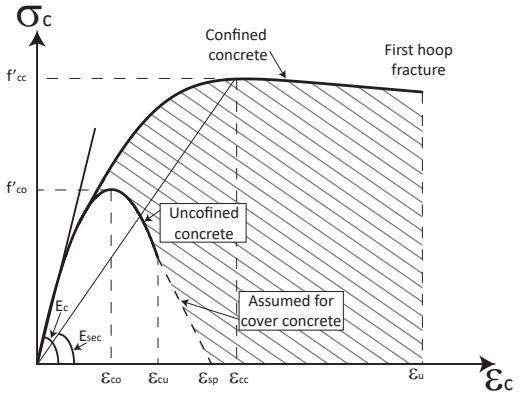

Fig. 10: Stress-strain diagram for concrete.

$$\sigma_c = \begin{cases} f_{co}^{'}\left[2\left(\frac{\varepsilon_c}{\varepsilon_{co}}\right) - \left(\frac{\varepsilon_c}{\varepsilon_{co}}\right)^2\right] & 0 \leq \varepsilon_c \leq \varepsilon_{co} \\ f_{co}^{'} & \varepsilon_{co} < \varepsilon_c \leq \varepsilon_{cu} \\ 0 & \varepsilon_c \geq \varepsilon_{cu} \end{cases} \tag{1}$$

3.2. Mechanical behaviour of steel

Hooke's law (Fig. 11a) describes the initial linear relationship between stress (σ_s) and strain (ε_s) for steel, known as elastic behavior. The Hooke's law is expressed by equation

(2), where , E_s, f_{sy}, ε_{sy} and ε_{su} denote the Young's modulus, yield strength, yield strain, and ultimate strain of the reinforcing steel, respectively. Additionally, Fig. 11b describes the steel hardening for different temperatures. In this sense, a reduction factor due to the temperature increase should be considered in the analysis.

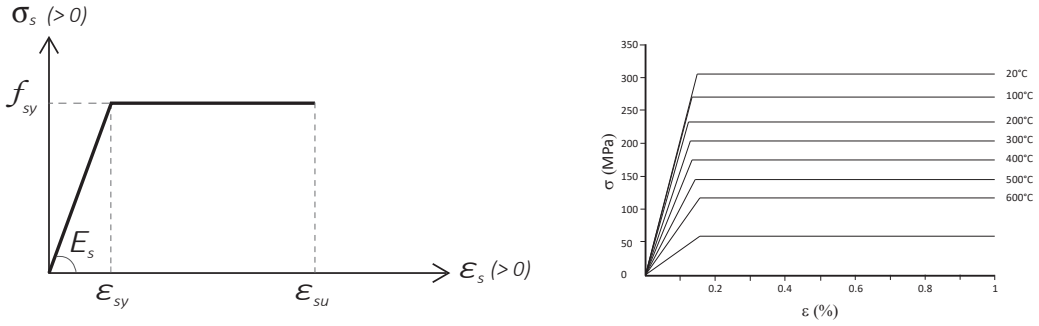

(a) Stress-strain diagram (b) Steel hardening

Fig. 11: Mechanical behaviour of steel.

$$\sigma_s = \begin{cases} E_s \varepsilon_s & 0 \leq \varepsilon_s < \varepsilon_{sy} \\ f_{sy} & \varepsilon_{sy} \leq \varepsilon_s < \varepsilon_{su} \end{cases} \tag{2}$$

3.3. Mechanical behaviour of FRP

FRP materials typically exhibit a linear elastic behavior straight through to failure without a distinct yield point ([40]). In this context, the material does not undergo plastic deformation before breaking, resulting in a straight line (stress-strain) until rupture (Fig. 12). The relationship can be described by a modified form of Hooke's Law (Eq. 3), where σ_f, E_f, ε_f and ε_{fu} denote the tensile strength, elastic modulus, strain, and peak strain of the FRP sheet, respectively.

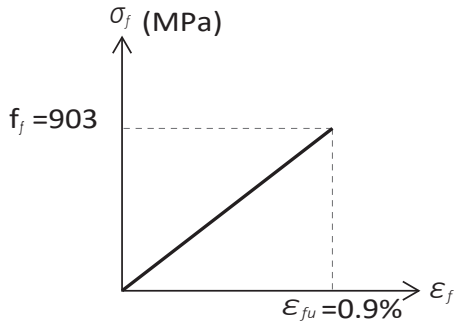

Fig. 12: Stres-strain diagram for FRP [35].

$$\sigma_f = \varepsilon_f E_f \qquad \varepsilon_f \leq \varepsilon_{fu} \tag{3}$$

3.4. Strain compatibility

The fundamental assumption in the analysis of RC beams reinforced with FRP is that the RC beam and FRP strip strain together. Thus, strain compatibility ensures a consistent strain across the interface, and the composite system operates cohesively as a unified material. Fig.13 presents the cross-section dimensions and material placement within it. It also shows the strain distribution over the cross-section. Therefore, the strain compatibility is defined by equations 4(a), (b), (c), (d).

$$\varepsilon_s^{'} = \varepsilon_c \ \frac{y_n - d_s^{'}}{y_n} \tag{4a}$$

$$\varepsilon_s = \varepsilon_c \ \frac{d_s - y_n}{y_n} \tag{4b}$$

$$\varepsilon_f = \varepsilon_c \ \frac{d_f - y_n}{y_n} \tag{4c}$$

$$\varepsilon_r = \varepsilon_c \ \frac{y_t}{y_n} \tag{4d}$$

where ε_c is the maximum compressive (crushing) strain of concrete, $\varepsilon_s^{'}$ and ε_s are the strains in the tension and compression steel bars, respectively, ε_f is the strain in the FRP strips, ε_r is rupture strain of concrete, d_s is the distance from the top surface to the centre of tension reinforcement, $d_s^{'}$ is the distance from the top surface to the centre of compression reinforcement, d_f is the distance from the top surface to the centre of FRP, y_n is the depth of neutral axis of concrete section, y_t is the distance from the neutral axis to the extreme fibre of the tension side, and $y^{'}$ is the distance from the neutral axis to the extreme fibre of the compression side.

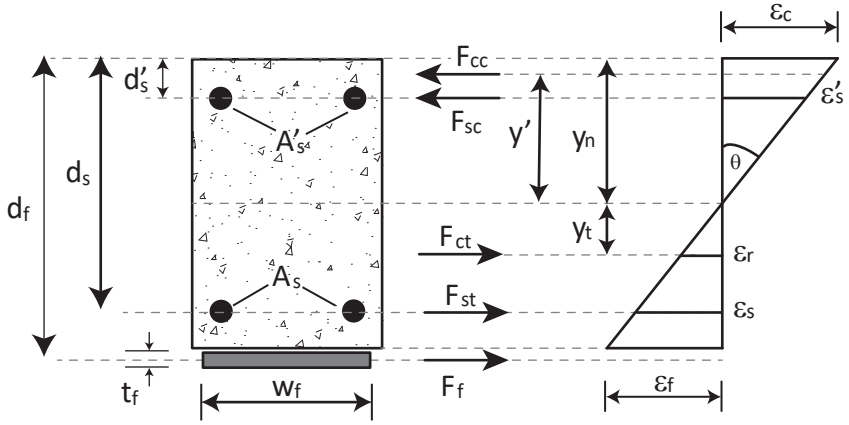

Fig. 13: RC beam reinforced with FRP: compatibility and equilibrium conditions.

3.5. Equilibrium conditions

Fig 13. and eq. (5) describe the equilibrium of the internal forces in the cross-section under the application of bending moment. Where F_{cc} is the force of concrete in compression, F_{ct} is the force of concrete in tension, F_{sc} is the force of steel in compression, F_{st} is the force of steel in tension, and F_f is the force of FRP.

$$\sum F = F_{cc} - F_{ct} + F_{sc} - F_{st} - F_f = 0 \tag{5}$$

The equation 7 represents an adapted form of equation 5, omitting concrete's tensile strength due to its low tensile strength (about 10% of its compressive strength). On the other hand, equation 6 substitutes the compressive force of concrete. Furthermore, the forces of steel and FRP are expressed on an equivalent basis using the normal stress concept.

$$F_{cc} = \int_0^{y_n} b\,\sigma_c\,y'\,dy' \tag{6}$$

$$\int_0^{y_n} b\,\sigma_c\ (y')\,dy' + f_{sc}^{'}A_{sc} - f_{sy}A_{st} - \sigma_f A_f = 0 \tag{7}$$

where $f_{sc}^{'}$ is the compressive strength of steel reinforcement, f_{sy} is the yielding strength of steel reinforcement, b is the width of beam. While A_{sc}, A_{st} and A_f are area of compression, tension of steel reinforcement, and FRP, respectively.

The internal moment acting on the cross-section must match the moments produced by internal forces about the neutral axis, as given by Eq. 8.

$$M = \int_0^{y_n} b\,\sigma_c\ (y')\,y'dy' + f_{sc}^{'}A_{sc}\left(y_n - d_s^{'}\right) - f_{sy}A_{st}\,(d_s - y_n) - \sigma_f A_f\,(d_f - y_n) \tag{8}$$

Substituting Eq. (1) through (4) into Eq. (7), the equilibrium conditions can be redefined in terms of the strains and Young's modulus of the materials, the distances from each material's centroid to the neutral axis, the dimensions of beam, and the details of the reinforcement. Within this framework, Eq. (7) exhibits its nonlinearity due to the mechanical behavior of concrete, strain compatibility, equilibrium requirement, and other factors. Therefore, the analytical procedure initiates with selecting a small value of ε_c.

For each ε_c , an initial y_n value is assumed, and iterated through the internal force equilibrium is reached. Then, the ε_c is gradually increased, continuing this iterative process for each new value. Finally, the analysis concludes upon satisfying the criteria outlined in Eq. (9 (a), (b)).

$$\varepsilon_c = \varepsilon_{cu} \tag{9a}$$

$$\varepsilon_f = \varepsilon_{fu} \tag{9b}$$

Once the parameters outlined in the preceding section are acquired, the moment M and the curvature θ can be determined by Eq. (8), (10), respectively. In a technical sense, each M value corresponds to a specific θ value. Consequently, this procedure allows for the construction of the moment-curvature diagram.

$$\theta = \frac{\varepsilon_c}{y_n} \tag{10}$$

3.6. Bond performance of external strengthening

Debonding can be defined as detrimental to the interfacial adhesion between FRP and concrete matrix. Generally, this is almost present in the failure mode of externally bonded fiber-reinforced strengthening systems. Numerous researchers have investigated theoretical, empirical, and numerical models about behavior debonding adhesively bonded fiber-reinforced polymers (FRP) sheets to a concrete substrate. The mathematical expressions that define these models correlate with different variables. The debonding and effective bond length models introduce the relationship between the effective bond length and the debonding load. Table 3 lists some of the existing models.

Table 3: FRP-concrete bond models

Reference	Relationships
Tanaka [41]	$F_{ub} = b_f L_b \left(6.13 - ln\left(L_b\right)\right)$
Hiroyuki and Wu [42]	$F_{ub} = b_f L_b \left(5.88 \left(0.1 L_b\right)^{-0.669}\right)$
Maeda et al. [43]	$F_{ub} = \left(110.2 \cdot 10^{-9} E_f t_f\right) b_f L_e$ $L_e = e^{6.13 - 0.58\, ln\, 0.001 E_f t_f}$
Taljsten [44]	$F_b = \sqrt{\frac{2 E_f t_f G_f}{1+\alpha_T}} b_f$ $\alpha_T = \frac{E_f t_f}{E_c t_c}$, $G_f = 0.14 f_c' \left(G_f = 0.65 \text{ if } f_{cm} > 46.2\right)$
Dai et al. [45]	$F_{ub} = \left(b_f + 7.4\right) \sqrt{2 E_f t_f G_f}$ $G_f = 0.524 f_c^{0.236}$
Brosens and van Germet [46]	$F_{ub} = 0.5 b_f L_b f_{ctm}$
Khalifa et al. [47]	$F_{ub} = \left(110.2 \cdot 10^{-9} \left(\frac{f_c'}{42}\right)^{\frac{2}{3}} E_f t_f\right) b_f L_e$ $L_e = e^{6.13 - 0.58\, ln\, 0.001 E_f t_f}$
Yang et al. [48]	$F_{ub} = 0.5 f_{ct} \left(0.5 + 0.08 \sqrt{\frac{E_f t_f}{100 f_{ctm}}}\right) L_e b_f$ $L_e = 100\ mm$
Adhikary and Mutsuyoshi [49]	$F_{ub} = 0.25 f_{cm}^{2/3} b_f L_e$

4. Results and observations

4.1. Thermal analysis

Transient thermal analysis was carried out to define the temperature gradient in the cross-section at a mid-span of 60 min after fire initiation (Fig.14, Fig.15). The results

were consistent with the data obtained from the set of thermocouples. Sixty minutes after fire initiation, the higher temperature gradient is located on the lower side. Technically, this occurs because there is exposure to a direct flame. The temperature gradient displays variations across the cross-section, where it gradually decays on the way to the upper side. Unsurprisingly, this temperature develops the lowest value. This is because the weight-loading kit works as insulation material.

In contrast, the other two sides are partially exposed to direct flame and directly exposed to warm air. As such, the threshold temperature is similar to the lower side. However, the temperature rapidly wanes on the way to the cross-section core.

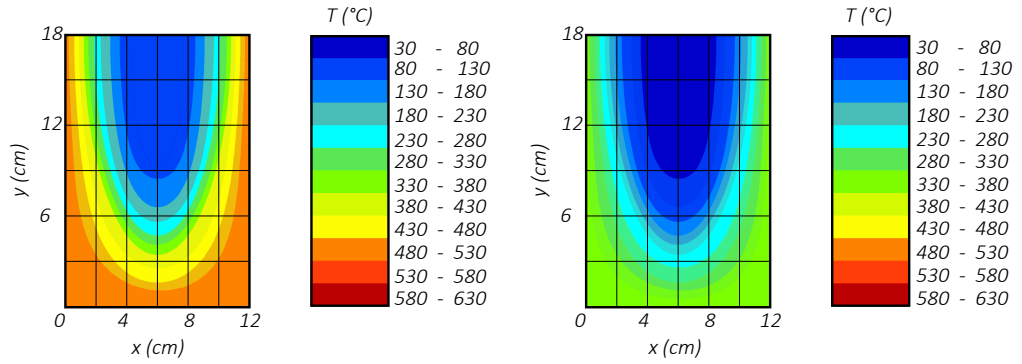

(a) Exp-B-y-a-01

(b) Exp-B-x-a-01

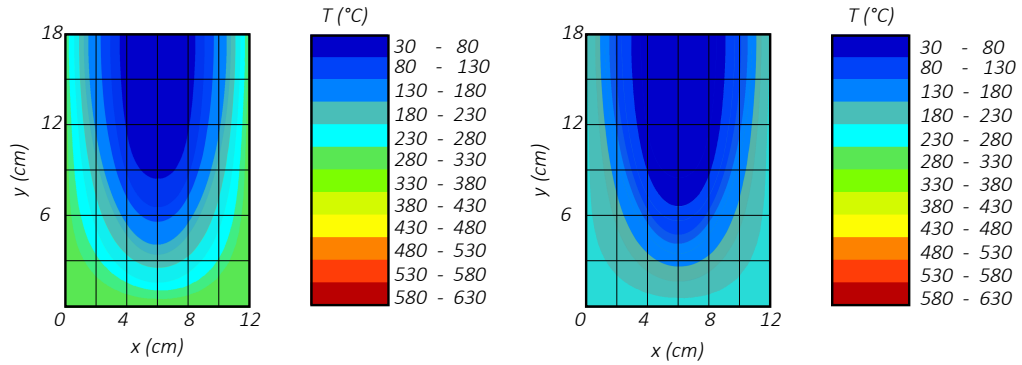

(c) Exp-A-y-a-02

(d) Exp-A-x-a-02

Fig. 14: Temperature distribution.

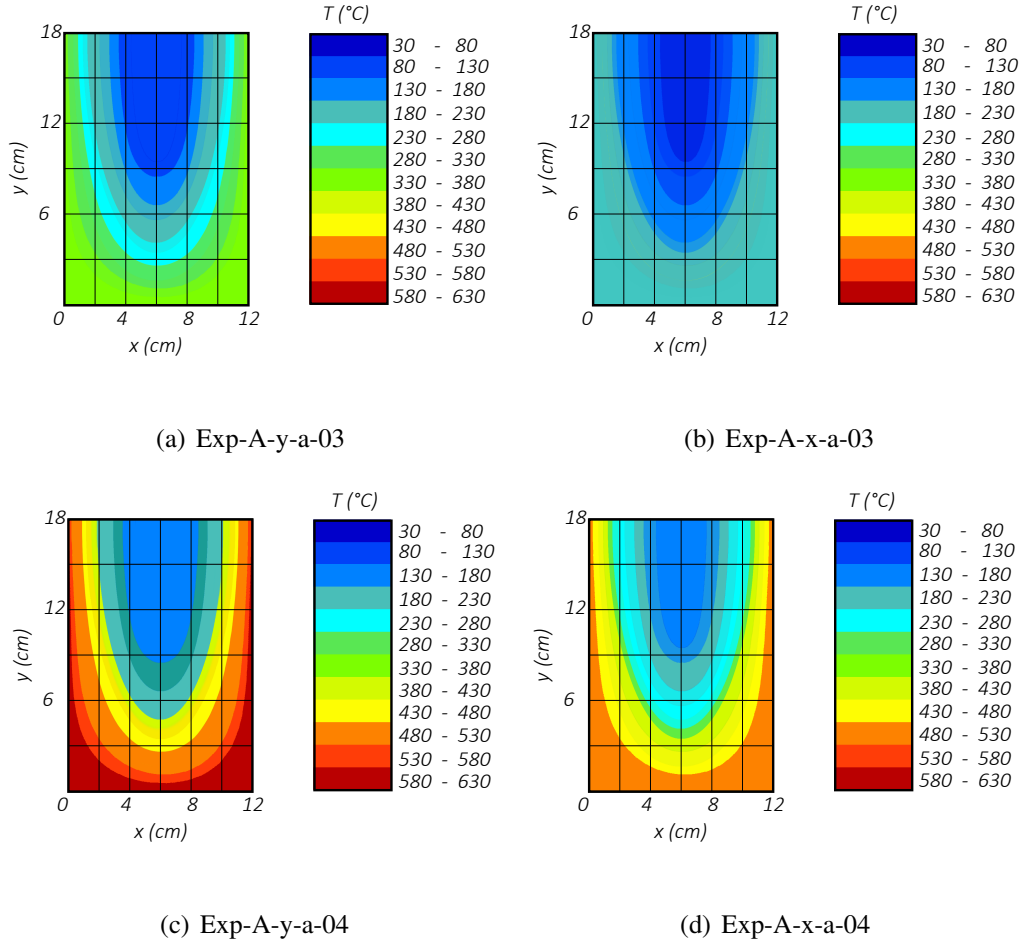

(a) Exp-A-y-a-03

(b) Exp-A-x-a-03

(c) Exp-A-y-a-04

(d) Exp-A-x-a-04

Fig. 15: Temperature distribution.

4.2. *Premature failure of the CFRP sheets*

The specimens labeled Exp-B-y-b and Exp-A-y-b (Figs. 16(a)-(b)), which were not subjected to elevated temperatures, exhibit the integrity of the concrete's surface finish and the effective bonding between the fibers and the concrete. Conversely, the specimens designated as Exp-A-y-a-02, Exp-A-x-a-04, and Exp-A-y-a-04 (Figs. 16(c)-(e)) display various forms of distress attributable to the effects of elevated temperatures. Through the image sequence depicted in Figures 16(a)-(f), it is feasible to compare the state of damage to CFRP strips resulting from exposure to high temperatures.

The specimens Exp-A-y-a-02 underwent the burning sequence 02, reaching temperatures from 330 to 380 °C. In this sense, Fig. 16c exhibits a slight thermal degradation, leading to a notable debonding at the end of CFRP laminates. Additionally, the thermal effects of fire caused the presence of thermal-induced interfacial voids within the adhesive layer, consequently leading to a decrease in bond strength. It can be primarily attributed to the differential thermal expansion of the materials. Meanwhile, the specimen Exp-A-x-a-04 was exposed to temperatures from 480 to 530 °C, showing a marked debonding at the end of the strips without any evidence of the thermal-induced interfacial voids within the adhesive layer (Fig. 16d). This observation suggests that the U-shaped insulation jacket mitigated the thermal degradation at the adhesive interface of Exp-A-x-a-04, preventing the formation of interfacial voids. Furthermore, specimen (Exp-A-y-a-04) left uncovered by an insulation jacket and subjected to temperatures exceeding 580 °C exhibited complete thermal degradation and delamination of the CFRP strips (Fig. 16e). As a result, the structural reinforcement provided by the CFRP laminates was entirely negated. Therefore, extreme thermal conditions severely compromised the integrity and functionality of the CFRP enhancements, resulting in a significant deterioration of the structural response of the specimen (Fig. 16f).

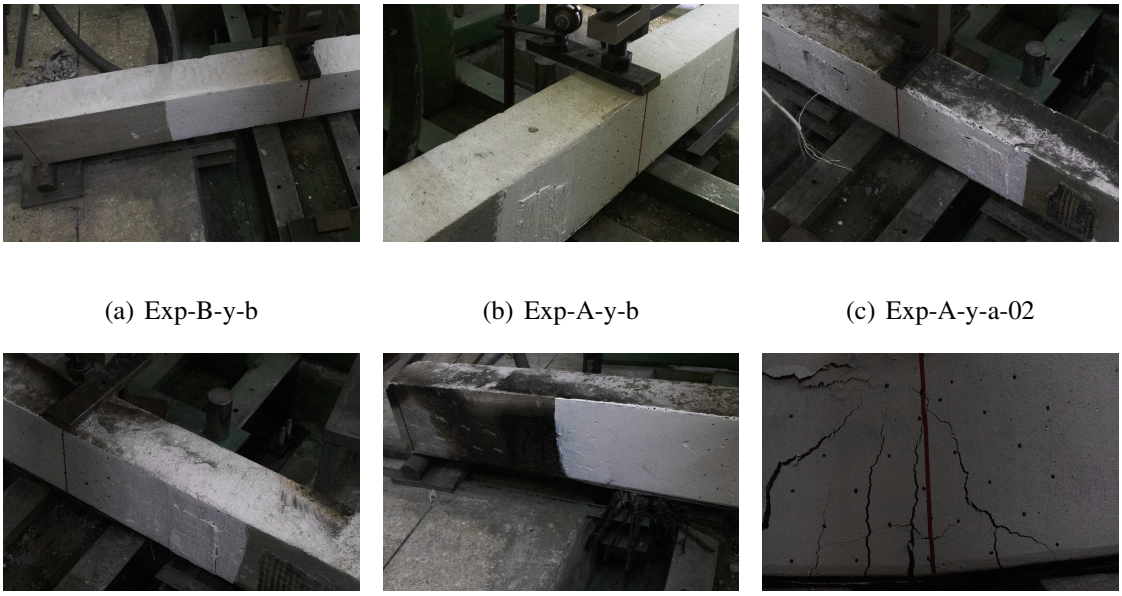

(a) Exp-B-y-b (b) Exp-A-y-b (c) Exp-A-y-a-02

(d) Exp-A-x-a-04 (e) Exp-A-y-a-04 (f) Exp-A-y-a-04

Fig. 16: Premature failure of the CFRP sheets.

4.3. Cracking and failure mechanisms

Research over half a century has identified that RC beams' cracking and failure mechanism with FRP reinforcement comes in some forms: FRP rupture, intermediate crack (IC) debonding, critical diagonal crack (CDC) debonding, and CDC debonding with concrete cover separation. Although all of them can lead to considerable damage, they work in different ways. In this sense, Figs. 18 and 19 depict the cracking and failure mechanisms in the experimental trials at different bending moment levels.

Of all the experimental trials, the Exp-B-y-b specimen (control beam) is the only one that is neither reinforced nor exposed to elevated temperatures. It is worth noting that an initial flexural crack emerged and extended at the center of the span. After that, as the applied load was increased, one major flexural crack was formed and instantly propagated into a diagonal path away from the center of the specimen accompanied by multiple flex-

ural cracks. Technically, the specimen reached failure 25 s after the first crack emerged, reaching an ultimate bending moment of 0.82 tf-m (Figs. 18(g)-(i)). Additionally, the crushing of compressive concrete was slightly present at the end of the failure. Therefore, this specimen characterizes the failure mode of a standard RC beam. Therefore, this specimen will provide valuable information to reveal the influence of input variables in the propagation and final state of damage through the comparative analysis of each specimen.

In the post-heating phase, the image sequence of specimen Exp-A-x-a-02 (Fig. 18a) indicates that the CFRP-concrete interface was slightly debonded and did not present any marks of burning due to elevated temperatures. Afterward, 3 min 44 s after the test initiation, two types of cracking and failure mechanisms emerged for a bending moment of 0.7 tf-m. The former is the IC debonding in which two flexural cracks emerged at the tension zone. In contrast, the latter is the crushing of compressive concrete, which appeared in the compression zone. A particular fact is that IC debonding failure is triggered automatically after the cracks appear, as evidenced in Figs. 18(a)-(c). Conversely, the effects caused by the crushing of compressive concrete were present. Finally, specimen Exp-A-x-a-02 primarily failed by IC debonding failure, reaching an ultimate bending moment of 1.02 tf-m. Therefore, the crushing of compressive concrete marks shows that the CFRP laminates were not greatly affected by elevated temperatures and worked as expected because the specimen presents flexural cracks more prominent than the control beam. It infers in the increasing the bending moment with a percentage of 20% compared to the control beam.

Rather than triggering automatically after the cracks appear, Exp-A-y-b gradually fails through crack formation, propagation, and extension. The image sequence Figs. 18(d)-(f)

shows that cracking formation begins 4 min 12 s later than the Exp-B-y-b (control beam). In this sense, two flexural cracks emerged at the middle span for a bending moment of 1.33 tf-m. Once cracks formed, they slightly propagated and extended without considerably impacting the final damage, accompanied by the development of more flexural cracks around the middle span. However, a critical shear crack emerged soon after, and subsequently, it rapidly propagated and extended. Successively, it gradually widens as the applied load increases. Finally, the specimen reached the failure by splitting along the tension reinforcement accompanied by separating the concrete cover at the compression zone and the debonding in the interfacial adhesion between CFRP and concrete matrix.

After 60 minutes, burning sequence 02 generated a temperature gradient range of 280-330 °C in the cross-section of the specimen Exp-A-y-a-02. Visual observations show that the adhesive layer is slightly detrimental, and CFRP laminates show some marks of debonding and burning. The study´s findings reveal that one flexural crack emerges in the middle of the span. After that, it gradually propagated and extended following a path parallel to the vertical axis. Figs. 18(j)-(l) show that CFRP laminates delayed the yielding of the longitudinal steel bars and extended the elastic regime. Subsequently, another flexural crack emerged, accompanied by a shear crack. As the applied load increased, all cracks rapidly widened. Finally, the specimen failed due to splitting along the tension reinforcement accompanied by wide cracks and effects of crushing concrete at the compression zone.

The specimens Exp-A-x-a-04 and Exp-A-y-a-04 were subject to burning sequence 04, reaching temperatures over 500 °C. In this sense, the specimen Exp-A-x-a-04 exhibits a failure mechanism based on the onset flexural crack at the middle of the span. After this

crack began to propagate and widen, multiple cracks emerged and rapidly propagated, reaching the failure by splitting along the tension reinforcement. The specimen Exp-A-ya-04 exhibits a similar failure mechanism; however, the multiple cracks took a while to emerge. By comparison of Figs. 19(a)-(c) and Figs. 18(m)-(o), the results show that although the insulation material does not work as expected due to detrimental in the adhesive layer after fire exposure, it contributes to delay the yielding of the longitudinal steel bars and increases the strength of Exp-A-x-a-04.

After exposing the specimen Exp-B-x-a-01 to over 400 °C for 60 minutes, visual observations show that the adhesive layer surpassed its glass transition temperature. Hence, the adhesive layer gradually began to deteriorate and caused a severe debonding between the insulation material and specimen. In this sense, the fire protection material did not work as expected, leaving the beam vulnerable to the effects of elevated temperatures. In the overall response of the specimen Exp-B-x-a-01, one flexural major crack evolved at the middle of the span, adopting a path parallel to the vertical axis (Figs. 19(d)-(f)). Additionally, a sizeable crack associated with the crushing of the concrete cover at the compression zone emerged 44 seconds after the onset of the first crack. Before reaching the failure, both cracks abruptly widen in less than 30 seconds as the applied load increases (Fig. 19(e)).

Fig. 17 shows the combining effects of CFRP reinforcement, fire protection material, and different temperature levels subjected to the strengthening effect. The ultimate bending moment and width crack were normalized concerning the control beam. Generally, increasing the temperature levels diminishes the strengthening and impact in the width cracks formation. However, if the specimens were protected with an insulation material,

the strength is enhanced qualitatively, accompanied by width crack formation. Moreover, the effects of crushing at compressive concrete are markedly witnessed as the width cracks do not exceed 175% compared with the control beam.

The physics governing failure mechanics makes it almost impossible for different scenarios to define exactly how the cracks propagate theoretically. Hence, the obtained results revealed the following findings: a) for ambient temperatures, the FRP reinforcement caused the critical crack to develop an increase in the propagation angle from 60º to 67º and the crack propagation changes in shape from straight to undulate, as displayed Figs. 18i and 18l; b) for elevated temperatures, the FRP reinforcement caused the critical crack to develop an increase in the propagation angle from 56º to 73º, and the crack propagation maintains its shape as undulate, as displayed in Figs. 18o and 19f; c) the fire protection material does not influence the propagation angle, maintaining an angle between approximately 80º and 82º d) the elevated temperatures caused the critical crack to propagate as an undulate shape.

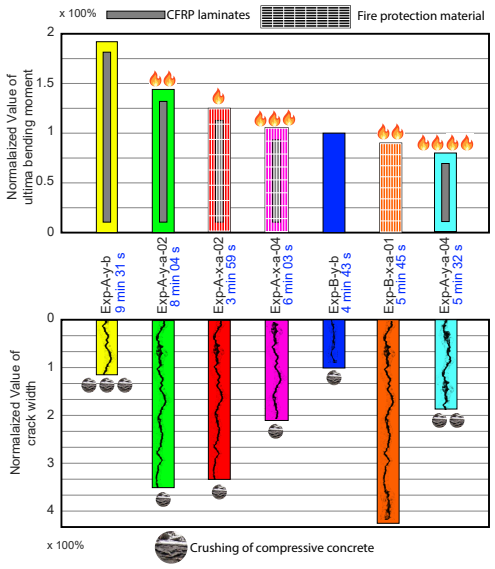

Fig. 17: Ultimated bending moment and width crack normalization.

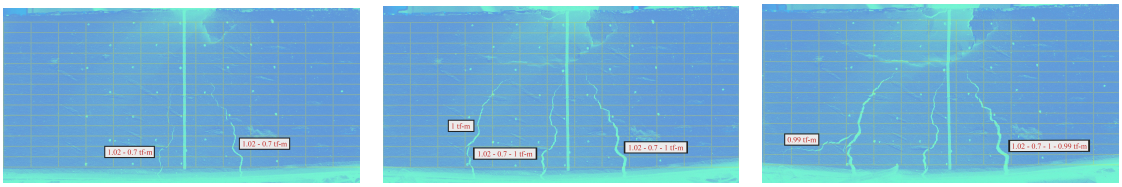

(a) Exp-A-x-a-02 (3 min 44 s) (b) Exp-A-x-a-02 (3 min 54 s) (c) Exp-A-x-a-02 (3 min 59 s)

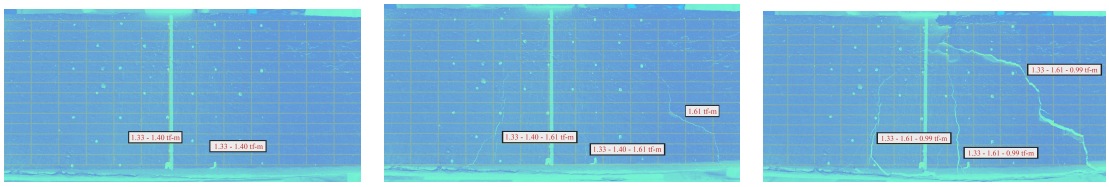

(d) Exp-A-y-b (7 min 56 s) (e) Exp-A-y-b (9 min 16 s) (f) Exp-A-y-b (9 min 31 s)

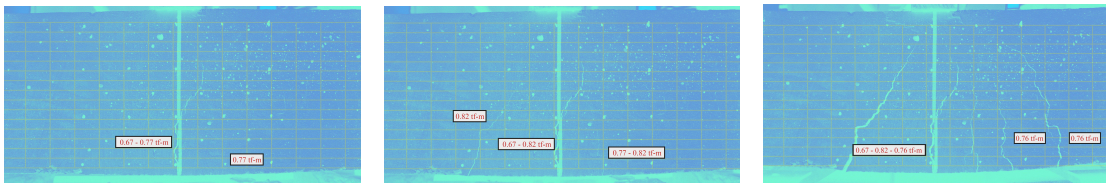

(g) Exp-B-y-b (4 min 18 s) (h) Exp-B-y-b (4 min 28 s) (i) Exp-B-y-b (4 min 43 s)

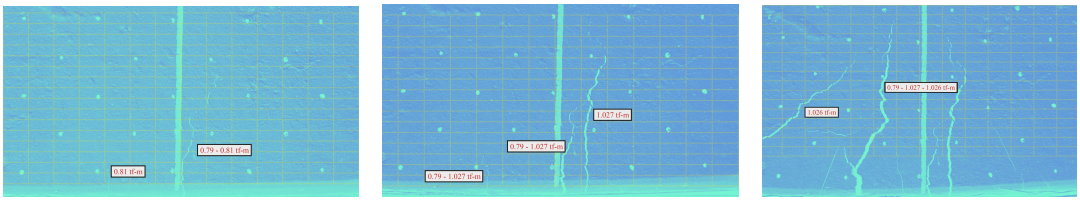

(j) Exp-A-y-a-02 (6 min 14 s) (k) Exp-A-y-a-02 (7 min 54 s) (l) Exp-A-y-a-02 (8 min 04 s)

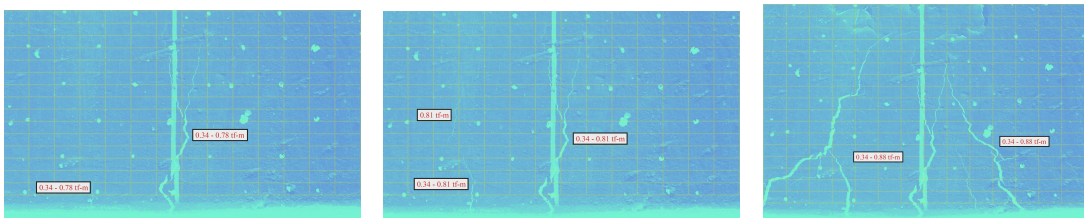

(m) Exp-A-x-a-04 (5 min 03 s) (n) Exp-A-x-a-04 (5 min 08 s) (o) Exp-A-x-a-04 (6 min 03 s)

Fig. 18: Crack progress of specimens.

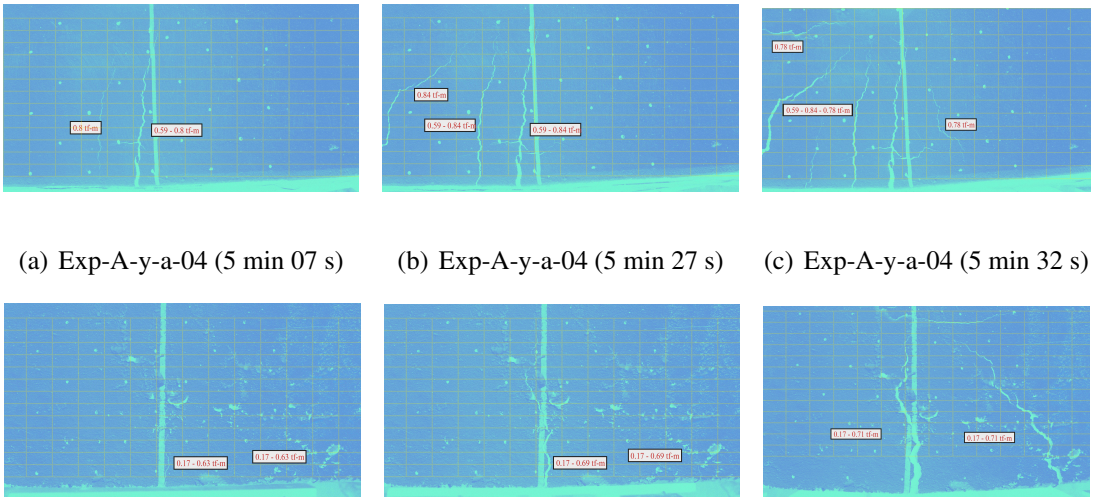

(a) Exp-A-y-a-04 (5 min 07 s) (b) Exp-A-y-a-04 (5 min 27 s) (c) Exp-A-y-a-04 (5 min 32 s)

(d) Exp-B-x-a-01 (5 min 01 s) (e) Exp-B-x-a-01 (5 min 20 s) (f) Exp-B-x-a-01 (5 min 45 s)

Fig. 19: Crack progress of specimens.

4.4. Moment-curvature diagram analysis

The moment-curvature diagrams describe the structural elements' flexural, deformation, and energy consumption behaviour. Some diagrams are similar to a theoretical shape, while others tend to flatten in their plastic region. Thus, characterizing them with their respective transitions (the yielding and ultimate points) is indispensable to defining the strength and serviceability of structural elements. The yielding point marks the triggering of large deformation and emerging cross-section damage. The highest point of the curve marks the ultimate point before that element reaches failure. Therefore, those points represent the transition from yielding the first longitudinal steel bars - crushing concrete - plastic deformation - failure.

By looking at the collection of all possible moment-curvature diagrams of the experimental trials (Fig. 20), we find that the control beam (blue curve Exp-B-y-b) represents the diagram moment-curvature of a standard RC beam. Therefore, this specimen will pro-

vide valuable information to reveal the influence of input variables in the final structural response through the comparative analysis of each curve.

The yellow curve (Exp-A-y-b) reached the highest tensile strength compared to the others. It means the ultimate bending moment is enhanced by 92% concerning the blue one. Additionally, the energy consumption in the unit length of the RC section (the area under the moment-curvature plot) is another indicator that shows the total energy the RC section can consume. The yellow curve translated into energy consumption indicates that it only absorbed 27% compared to the blue curve (Fig. 20). Those results reveal that the specimen Exp-A-y-b acquired a notable brittle behaviour, showing the strength and serviceability of an RC beam reinforced with CFRP. It is because the Exp-A-y-b specimen was reinforced with CFRP and not exposed to fire, which directly infers the fibres' work to its total capacity.

The green curve (Exp-A-y-a-02) exhibits exemplary ductile behaviour through the highest area under the moment-curvature plot (dissipation energy), which is 35% higher than the blue curve (Fig. 20). Additionally, the specimen Exp-A-y-a-02 developed the highest plastic energy and attained an ultimate bending moment 44% greater than the control beam (blue one). The most striking fact is the variations of tendency curves where the green one depicts ductile behaviour, while the yellow one shows brittle behaviour. Therefore, the failure mechanism is susceptible to slightly changing one or more input variables.

From a technical point of view, the tendency of the red curve (Exp-A-x-a-02) reveals essential hints about the impact of elevated temperatures on the specimens' mechanical properties. First, the moment-curvature diagram (Fig. 20) is split into three stages. The

first stage begins with the applied load starting to be transmitted to the specimen, and the first flexural crack emerges. The linear relationship (first stage's slope) of red and blue curves is almost similar in this stage. The second stage is from the first flexural crack emerging to steel yielding. In this stage, the CFRP delayed the trigger of the steel yield of Exp-A-x-a-02 (red curve). The third stage starts from the steel yielding point, reaching the ultimate bending moment to the failure point. In this stage, the flexural strength of the red curve experiments with an increment of 24% concerning the blue one. It infers that the contribution of CFRP laminates in the structural response is partial. This is because CFRP laminates presented marks of deterioration and burning. Therefore, elevated temperature caused the dissipation energy of the red curve (Exp-A-x-a-02) to be diminished by 80% compared to the blue one.

As analyzed in the previous section, the fire protection material of Exp-B-x-a-01 could not attenuate the effects of elevated temperatures so this trial can be considered as a standard RC beam under elevated temperatures. In this sense, the orange curve (Exp-B-x-a-01) exhibits a detrimental in its mechanical properties. It is evidenced by the decreasing of dissipation energy and ultimate bending moment in a 57% and 10% compared to the control beam (blue curve), respectively.

The moment-curvature diagram of the cyan curve (Exp-A-y-04) adopts a parabolic shape similar to a standard RC beam shape. It infers that the contribution of CFRP laminates is almost nonexistent. Thus, it is a marker of detrimental CFRP by burning because the specimen was not protected by insulation material. Comparing the cyan curve (Exp-A-y-04) and magenta curve (Exp-A-x-04) shows that both curves adopted the same parabolic shape, inferring that the insulation material was ineffective. Consequently, the

CFRP laminates did not work as expected due to their burning. Visual observations revealed the deterioration in the bond connection between the insulation material and the specimen due to direct fire exposure.

Additionally, The magenta and cyan curves of Fig. 20 reveal that the first stage's slope (pre-cracking) is almost similar, inferring that both specimens maintained the same elastic regime. Conversely, the second stage's slope (cracking) changed considerably, where the dissipation energy decreased by 18% and 40%, and the ultimate bending moment increased by 5% and decreased by 21% for the magenta and cyan curves, respectively. It infers that the insulation material only protected from fire in the first instance of the heating phase and after that was ineffective due to inexistent thermal resistance. Consequently, elevated temperature causes detrimental effects on the adhesion properties between the CFRP and the specimen, so the debonding effects should be accounted for.

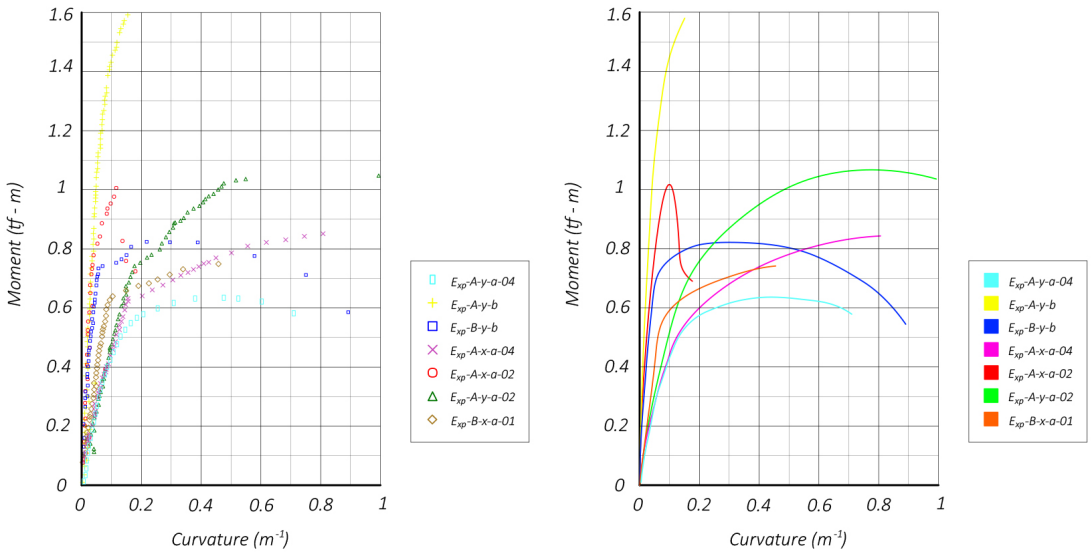

(a) Scatter plot (b) Curve plot

Fig. 20: Experimental moment-curvature diagram.

After several failed attempts to obtain an analytical model through computation (Figs. 21(a)-(d)), the patterns, regularities, and relationships that emerged from the moment-curvature graph are inconsistent with theory. This could occur because the deterioration in the mechanical properties was not uniform, and subsequently it infers the onset of some adverse effects generating limitations in the modelling. For example, the thermal gradient directly inferred in a shift of the line of action of internal force (moving towards the cold side) causes the bending moment to inverse; change in the chemical composition of the concrete, suppose a nonhomogeneity in the microstructure of it, resulting in abnormalities in the relationships between the strength and modulus of elasticity. The surface of specimens that present discolouring is vulnerable to the forming, triggering, and gradual propagation of multiple cracks.

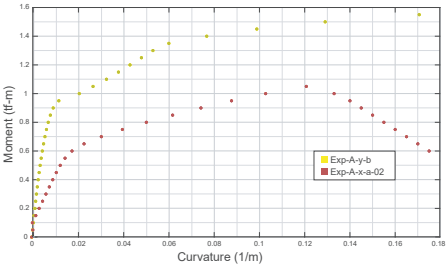

(a) Scatter plot

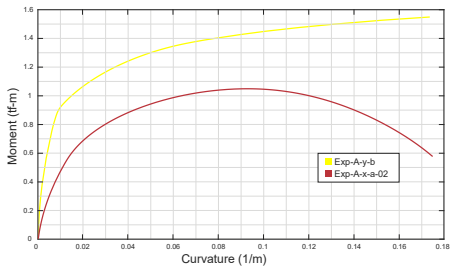

(b) Curve plot

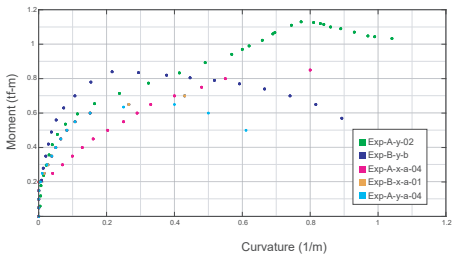

(c) Scatter plot

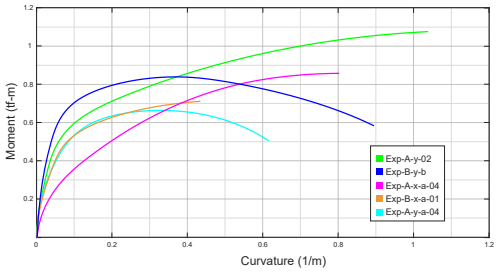

(d) Curve plot

Fig. 21: Analytical moment-curvature diagram.

The comparison of moment and curvature at the transition points (yielding and ultimate) between experimental results and predictions from the analytical model are summarized in Table 4. The prediction of the analytical model presents a high accuracy at the ultimate moment. In contrast, the prediction differs from the experimental one at the yielding moment, especially for the beams without a thermal insulation board. This distortion can be attributed to the degradation of individual mechanical properties of each material and their interaction between them.

Table 4: Results comparison.

Specimen	**Study**	M_y $(tf-m)$	θ_y (m^{-1})	M_u $(tf-m)$	θ_u (m^{-1})
	Exp.	0.408	0.09	0.647	0.415
A-y-a-04	Theo.	0.4	0.065	0.655	0.386
	Error (%)	1.96%	27.78%	1.24%	6.99%
	Exp.	0.464	0.104	0.862	0.833
A-x-a-04	Theo.	0.378	0.084	0.865	0.775
	Error (%)	18.57%	19.54%	0.29%	6.92%
	Exp.	1.42	0.094	1.595	0.159
A-y-b	Theo.	0.89	0.087	1.53	0.163
	Error (%)	37.32%	7.45%	4.08%	2.52%
	Exp.	0.612	0.044	0.833	0.258
B-y-b	Theo.	0.591	0.049	0.843	0.303
	Error (%)	3.53%	13.18%	1.28%	17.48%
	Exp.	0.706	0.041	1.03	0.113
A-x-a-02	Theo.	0.6	0.034	1.037	0.096
	Error (%)	15.01%	17.07%	0.68%	15.04%
	Exp.	0.705	0.164	1.08	0.828
A-y-a-02	Theo.	0.6	0.095	1.06	0.95
	Error (%)	14.89%	42.07%	1.85%	14.73%

5. Conclusions

The experiment (Exp-A-y-b) reveals that the CFRP reinforcement increases considerably the ultimate strength and stiffness capabilities. Additionally, they have the potential to heal partially cracks. The final state damage of specimens reinforced with CFRP and not exposed to fire shows a crack map where a widened shear crack emerged at the sides of the specimens accompanied by multiple flexure cracks at the middle of the span, separating the concrete cover at the compression zone and the debonding in the interfacial adhesion between CFRP and concrete matrix. Therefore, if the state of damage of specimen exposure to elevated temperatures presents similar characteristics, the insulation material works as expected. Consequently, the interfacial adhesion between it and the specimen is not detrimental.

The observations were taken for experimental trials over 400 °C. Thus, these trials aimed to reach a detrimental effect on the concrete surface instead of determining the temperature threshold that induces changes in the chemical composition of concrete. Additionally, the CFRP material has no thermal insulation capacity, so the damage at the surface of the concrete does not alter the presence of this or not. 400 °C is enough to cause severe damage in the adhesive layer, consequently inferring the debonding between CFRP/concrete. Subsequently, the superposition of damages induces the creation of notches at the FRP-concrete interface. These notches would be derived as the tips of the crack that immediately trigger failure by IC debonding. Therefore, IC debonding is the predominant failure for the specimens associated with CFRP reinforcement.

The bending moment fluctuations and image sequences captured by instrumentation of experimental trials reveal the work sequence of the reinforced steel bars, concrete,

and CFRP and the impact of those materials on the final damage. Therefore, the results obtained in Figs. 18, 19 and Fig. 20 show that some damage patterns, such as brittle behaviour (Exp-A-y-b and Exp-A-x-a-02), are directly related to the crushing of compressive concrete and curvature less than 0.1 m^{-1}; the transition between ductile to brittle failure is proportional to the time (from shortest to largest) in which the specimen reaches failure; the forming, triggering, and gradual propagation of multiple cracks are present in ductile failure, while the forming trigger and instant propagation of major cracks are present in brittle failure. Finally, the reinforcement effects of CFRP are completely diminished when the strips or layers show several debonding or burning after fire exposure.

Although the study conducted experimental trials in various settings, none of the specimens developed a failed type of mixed mode debonding. Remarkably, crack formation was predominant within the mid-span region rather than the shear span region. Moreover, this is because the three-point bending test induces a bending moment concentration along the mid-span region. Thus, there are some limitations to the study, mainly that the four-point bending test induces a different bending moment distribution. Therefore, such a test is indispensable for obtaining more conclusive results on whether the type of bending test is related to the debonding failure mode.

The observed damage patterns in the specimens indicate that the anchorage between the specimen and CFRP is a crucial concern. In this context, the study meticulously focused on the surface finish, irregularities at the end of CFRP strips, anchorage mechanism, and the anchorage length. Nevertheless, the findings do not provide conclusive hints that reveal the significance of each parameter in the reinforcement system's performance, durability, and reliability. Furthermore, when reinforcing real-life reinforced

concrete (RC) structural members with CFRP, it is crucial to consider various other aspects. Environmental factors, including exposure to UV light, moisture, and temperature variations, can significantly cause differences in the thermal expansion coefficients between CFRP and concrete substrate. A thermal incompatibility can induce stress at the interface, leading to insufficient bond strength. Stress concentration can occur at the ends of CFRP reinforcements and at points where the concrete substrate exhibits geometric discontinuities. This phenomenon emerges because the stress and strain distribution in these specific areas differ significantly from the bonded regions. Thus, reaching a surface finish with average surface roughness from 0 to 0.075 mils and avoiding irregularities at the end of CFRP is necessary to avoid stress concentration, thereby minimizing the risk of peeling and debonding. Anchorage mechanism, a well-designed anchorage and adequate anchorage length can significantly improve the load transfer capabilities between the FRP and concrete and ensure a more uniform stress distribution along the bonded interface, increasing the bond strength and reducing the risk of debonding.

References

[1] DESA UN. World urbanization prospects 2018: Highlights. 2019.

[2] Krishna D. A, Priyadarsini R. S, Narayanan S. Effect of elevated temperatures on the mechanical properties of concrete. Procedia Struct 2019; 14 384-394 doi:10.1016/j.prostr.2019.05.047.

[3] Al-rousan R. Impact of Internal CFRP strips on the flexural behavior of heat-damaged reinforced concrete beams. Heliyon 2023; 9 e17145 doi:10.1016/j.heliyon.2023.e17145.

[4] Khaliq W, Anis K. High temperature material properties of calcium aluminate cement concrete. Constr Build Mater. 2015; 94 475-487 doi:10.1016/j.aej.2023.06.086.

[5] Al-rousan R. Case Studies in Construction Materials The behavior of heated damaged shear-deficient RC beams reinforced internally with welded wire mesh. Case Stud. Constr. Mater. 2021; 15 687 doi:10.1016/j.cscm.2021.e00687.

[6] Zhao G, Li J, Han F, Shi M, Fan H. Sulfate-induced degradation of cast-in-situ concrete influenced by magnesium. Constr Build Mater. 2019; 199 194-206 doi:10.1016/j.conbuildmat.2018.12.022.

[7] Arioz O. Effects of elevated temperatures on properties of concrete. Fire Saf. J. 2007; 42 516-522 doi:10.1016/j.firesaf.2007.01.003.

[8] Georgali B, Tsakiridis P. Microstructure of fire-damaged concrete. A case study. Cem Concr Compos . 2005; 15 255-259 doi:10.1016/j.cemconcomp.2004.02.022.

[9] Al-rousan R. Anchored CFRP ropes for flexural capacity recovering of thermally damaged RC one-way slabs. Alex. Eng. J. 2022; 76 687 doi:10.1016/j.aej.2023.06.086.

[10] Al-rousan R. Influence of macro synthetic fibers on the flexural behavior of reinforced concrete slabs with opening. Civ. Eng. J. (Iran). 2021; 8 2001–2021 doi:10.28991/CEJ-2022-08-09-016.

[11] Jawdhari A, Fam A, Kadhim M.M.A. Thermal bowing of reinforced concrete sandwich panels using time-domain coupled-field finite element analysis. Eng. Struct. 2022; 252 113592 doi:10.1016/j.engstruct.2021.113592.

[12] Hajiloo H, Green M. F. GFRP reinforced concrete slabs in fire: Finite element modelling. Eng. Struct 2019; 183 1109-1120 doi:10.1016/j.engstruct.2019.01.028.

[13] Siddika A, Al Mamun M. A, Alyousef R, Mugahed Y. H. Strengthening of reinforced concrete beams by using fiber-reinforced polymer composites: A review. J. Build 2019; 25 384-394 doi:10.1016/j.jobe.2019.100798.

[14] Amini Pishro A, Zhang Z, Amini Pishro M, Liu W, Zhang L, Yang Q. Structural performance of EB-FRP-strengthened RC T-Beams subjected to combined torsion and shear using ANN. Materials 2022; 221 (15): 4852 doi:10.3390/ma15144852.

[15] Sharifianjazi F, Zeydi P, Bazli M, Esmaeilkhanian A, Rahmani R, Bazli L, Khaksar S. Fibre-reinforced polymer reinforced concrete members under elevated temperatures: A review on structural performance. Polymers 2022; 14 (3): 472 doi:10.3390/polym14030472.

[16] Chen X, Wang Z, Li X, Leng Y, Harries K.A, Xu Q. Torsional strengthening using carbon fiber reinforced polymer of reinforced concrete beams subject to combined bending, shear and torsion. Adv. Struct. Eng. 2023; 26 (2): 272-286 doi:10.1177/13694332221124624.

[17] Mehran A, Ronagh H, Dux P. Behavior of FRP strengthened reinforced concrete beams under torsion. J. Compos. Constr. 2007; 11 192–200 doi:10.1061/(asce)1090-0268(2007)11:2(192).

[18] Godat A, Qu Z, Lu X. Size effects for reinforced concrete beams strengthened in shear with cfrp strips. J. Compos. Constr. 2010; 3 260–271 doi:10.1061/(asce)cc.1943-5614.0000072.

[19] Mostofinejad D, Shameli S. Externally bonded reinforcement in grooves (EBRIG) technique to postpone debonding of FRP sheets in strengthened concrete beams. Constr Build Mater. 2013; 38 751–758 doi:10.1016/j.conbuildmat.2012.09.030.

[20] Golias E, Zapris A, Kytinou V, Kalogeropoulos G, Chalioris C, Karayannis C. Effectiveness of the novel rehabilitation method of seismically damaged rc joints using c-frp ropes and comparison with widely applied method using c-frp sheets - experimental investigation. Sustainability 2021; 13 doi:10.3390/su13116454.

[21] Sabzi J, Esfahan M, Ozbakkaloglu T, Farahi B. Effect of concrete strength and longitudinal reinforcement arrangement on the performance of reinforced concrete beams strengthened using EBR and EBROG methods. Eng. Struct. 2020; 205 doi:10.1016/j.engstruct.2019.110072.

[22] Zapris A, Naoum M, Kytinou V, Sapidis G, Chalioris C. Fiber reinforced polymer debonding failure identification using smart materials in strengthened T-shaped reinforced concrete beams. Polym. J. 2023; 15 doi:10.3390/polym15020278.

[23] Zaki M, Rasheed H. Behavior of reinforced concrete beams strengthened using CFRP sheets with innovative anchorage devices. Eng. Struct 2020; 215 doi:10.1016/j.engstruct.2020.110689.

[24] GangaRao V. S, Vijay P. V. Bending behavior of concrete beams wrapped with carbon fabric. J. Struct. Eng. 1998; 124 3–10 doi:10.1061/(asce)0733-9445(1998)124:1(3).

[25] Klamer E. L, Influence of temperature on concrete beams strengthened in flexure with CFRP. Thesis, TU Eindhoven, The Netherlands 2009.

[26] Bazli M, Bazli M, Mechanical properties of fibre reinforced polymers under elevated temperatures: An overviewe. Polym 2020; 12 1–31 doi:10.3390/polym12112600.

[27] American concrete Institute ACI. Guide for the design and construction of externally bonded frp systems for strengthened concrete structure. Farmington Hills, MI, USA 2017.

[28] International Federation for Structural Concrete. Externally applied FRP reinforcement for concrete structures. Lausanne, Switzerland 2019.

[29] Michels J, Czaderski C, Motavalli M. Glass transition evaluation of commercially available epoxy resins used for civil engineering applications. Compos. B. Eng. 2015; 77 484–493 doi:10.1016/j.compositesb.2015.03.053.

[30] Pereira M, Soares A, Flores I, Correia J. Influence of exposure to elevated temper-

atures on the physical and mechanical properties of cementitious thermal mortars. Appl. Sci. 2020; 10 doi:10.3390/app10062200.

[31] Zhang H. Y, Lv H. R, Kodur V, Qi S. L. Comparative fire behavior of geopolymer and epoxy resin bonded fiber sheet strengthened RC beams. Fire Saf J 2018; 155 86-94 doi:10.1016/j.engstruct.2017.11.027.

[32] Kodur V, Bhatt P, Naser M. High temperature properties of fiber reinforced polymers and fire insulation for fire resistance modeling of strengthened concrete structures. Compos. B. Eng. 2019; 175 107104 doi:10.1016/j.compositesb.2019.107104.

[33] Naser M.Z, Hawileh R. A, Abdalla J. A. Fiber-reinforced polymer composites in strengthening reinforced concrete structures: A critical review. Eng. Struct 2019; 198 109542 doi:10.1016/j.engstruct.2019.109542.

[34] Al-Zaid R, Rajeh Z. Al-Negheimish A., Al-Saawani M., Analytical study on RC beams strengthened for flexure with externally bonded FRP reinforcement. Compos. B. Eng. 2012; 2 129–141 doi:10.1016/j.compositesb.2011.11.015.

[35] TYFO ® . TYFO ® SCH-41 Composite using Tyfo ® S Epoxy.

[36] Fernando P. R, Parvathakeetha A, Einon Mariya V. Producing Lightweight Concrete Using Tobacco Wastes. 1st Conference of CIDA Restore Project 2008.

[37] Costa D, Valença J, Julio E. Laboratorial test monitoring applying photogrammetric post-processing procedures to surface displacements. Meas. 2011; 44 527–538 doi:10.1016/j.measurement.2010.11.014.

[38] Comité Euro-International du Béton . Comite Euro-International - CEB FIP model code. 1990. ISBN 0727716964.

[39] Zhou Y, Liu S, Feng J, Fan H. Improved finite difference analysis of dynamic responses of concrete members reinforced with FRP bars under explosion. Compos. Struct. 2019; 230 111518 doi:10.1016/j.compstruct.2019.111518.

[40] Yuan C, Chen W, Pham T, Hao H, Chen L, Wang J. Experimental and analytical study of flexural behaviour of BFRP sheets strengthened RC beams with new epoxy anchors. Eng. Struct. 2021; 241 112441 doi:10.1016/j.engstruct.2021.112441.

[41] Tanaka T. Shear resisting mechanism of reinforced concrete beams with CFS as shear reinforcement.. Graduation Thesis, Hokkaido University Kitaku Japan 1996;

[42] Hiroyuki Y, Wu Z. Analysis of debonding fracture properties of CFS strengthened member subject to tension.. In Proceedings of the 3rd International Symposium on Non-Metallic (FRP) Reinforcement for Concrete Structures Sapporo, Japan 1997; 287 - 294

[43] Maeda T, Asano Y, Sato Y, Ueda T. A study on bond mechanism of carbon fiber sheet.. In Proceedings of the 3rd International Symposium on Non-Metallic (FRP) Reinforcement for Concrete Structures Sapporo, Japan 1997; 279 - 285

[44] Talijsten B. Strengthening of concrete prisms using the plate-bonding technique.. Int. J. Fract 1996; 82 253–266 doi:10.1007/BF00013161.

[45] Dai J, Ueda T, Sato Y. Development of the nonlinear bond stress–slip model of fiber reinforced plastics sheet–concrete interfaces with a simple method.. J. Compos. Constr. 2005; 9 52-62 doi:10.1061/(ASCE)1090-0268(2005)9:1(52).

[46] Brosens K. Anchoring stresses between concrete and carbon fiber reinforced laminates.. In Proceedings of the 3rd International Symposium on Non-Metallic (FRP) Reinforcement for Concrete Structures Sapporo, Japan 1997; 271 - 278

[47] Khalifa A, Gold W, Nanni A, Aziz A. Contribution of externally bonded FRP to shear capacity of RC flexural members. J. Compos. Constr. 1998; 2 195–202 doi:10.1061/(ASCE)1090-0268(1998)2:4(195).

[48] Yang Y, Yue Q, Hu Y. Experimental research on the bond performance of CFRP-concrete interface.. J. Build. Struct. 2001; 22 36–42

[49] Adhikary B, Mutsuyoshi H. Study on the bond between concrete and externally bonded CFRP sheet. In Proceedings of the 6th International Symposium on Fiber Reinforced Polymer Reinforcement for Concrete Structures (FRPRCS-5) Cambridge, UK 2001; 371 - 378